RSC Advances

PAPER

View Article Online
View Journal | View Issue

Cite this: *RSC Adv.*, 2019, **9**, 13981

Modulation of charged a_1/a_2 domains and piezoresponses of tensile strained $PbTiO_3$ films by the cooling rate

Jinyuan Ma,[abc] Yinlian Zhu,*[a] Yunlong Tang,[a] Mengjiao Han,[ad] Yujia Wang,[a] Ningbin Zhang,[ac] Minjie Zou,[ac] Yanpeng Feng,[ad] Wanrong Geng[ac] and Xiuliang Ma[ab]

Controlling domain width, orientation, and patterns in oxide ferroelectrics are not only important for fundamental research but also for potential electronic application. Here, a series of $PbTiO_3$ thin films under various cooling rates were deposited on (110)-oriented $NdScO_3$ substrates by pulsed laser deposition and investigated by using conventional transmission electron microscopy, Cs-corrected scanning TEM and piezoresponse force microscopy. Contrast analysis and electron diffraction revealed that $PbTiO_3$ films are a_1/a_2 domain patterns under large tensile strains with different cooling rates. The a_1/a_2 domains distribute periodically and the domain width increases with decrease in the cooling rates. Upon increasing the cooling rate, the domain density increases and the domain configurations become complicated. There are special square frame-like domain patterns with charged domain walls found in the PTO films with the fast cooling rate. PFM measurement shows that the PTO films with high cooling rate exhibit enhanced piezoresponse behavior which is ascribed to the high density domain/domain walls and special domain configurations. The formation mechanism of the different domain configurations is discussed in terms of the effect of cooling rates, defects and thermal kinetics. These results are expected to provide useful information for domain/domain wall control and thus facilitate further modulation of the properties for potential applications.

Received 2nd April 2019
Accepted 29th April 2019

DOI: 10.1039/c9ra02485a

rsc.li/rsc-advances

1. Introduction

Ferroelectric materials have been widely used and also show great potential in the electronics industry due to their excellent physical properties, such as ferroelectric, piezoelectric, dielectric and so on.[1] With the trend for electronic device miniaturization, ferroelectrics need to decrease their physical dimensions to broaden their applications. Along with the size decrease, the ferroelectric materials take the form of thin films, nanowires and even nanodots, which will introduce many influencing factors (such as residual stress due to epitaxy, surface tension, shape anisotropy or structural defects) on the physical properties.[2] The thin film ferroelectrics as the most promising materials for non-volatile memories have received much attention and their physical properties are highly correlated to the internal domain structure.[3,4] For example, previous studies indicate that a peculiar rumpled nanodomain structure is analogous to morphotropic phase boundaries in ultrathin $BiFeO_3$ films, while the switching of 90° domains can enhance the piezoelectric property in tetragonal ferroelectric thin films.[5,6] Moreover, the domain wall is a transition region between adjacent domains, which could give rise to emerging functionalities to the films, such as conduction, magnetotransport and photovoltaic effects.[7–9] Thus, it is necessary to understand the domain evolution mechanism for better control of domain patterns and may further modify the film properties.

Generally speaking, the thermodynamic equilibrium domain structure in a ferroelectric is determined by the minimization of the total free energy of the system, which is typically a sum of electrostatic energy, elastic strain energy, and domain wall formation energy.[10,11] In the case of ferroelastic domains in tetragonal ferroelectric perovskites, such as $PbTiO_3$ (PTO), $PbZr_{0.2}Ti_{0.8}O_3$, walls with {110} orientations are only permitted because of the tetragonal symmetry. In a film is grown on (001) orientation, the ferroelastic domain patterns consist of a- and c-domains whose *a* and *c* axes are normal to the growth plane, respectively. These are the so-called 90° a/c domain and a_1/a_2 domain.[12,13] In the past decades, great efforts have been made in the experimental explorations and theoretical simulations on various domain structures in ferroelectric thin films, such as c/a_1/a_2 multi-domains and full flux closure vortex domain

[a]*Shenyang National Laboratory for Materials Science, Institute of Metal Research, Chinese Academy of Sciences, Wenhua Road 72, 110016 Shenyang, China. E-mail: ylzhu@imr.ac.cn*

[b]*State Key Lab of Advanced Processing and Recycling on Non-ferrous Metals, Lanzhou University of Technology, Langongping Road 287, 730050 Lanzhou, China*

[c]*School of Material Science and Engineering, University of Science and Technology of China, Hefei 230026, China*

[d]*University of Chinese Academy of Sciences, Yuquan Road 19, 100049 Beijing, China*

structures.[14–19] Both theoretical and experimental studies indicate that the formation of domain structures in tetragonal PTO thin film depends on many factors. It has been reported that misfit strain between the film and substrate is a primary influence factor for the formation of domain pattern in the film. When the misfit strain changes from large compressive to large tensile strain, the domain develop from c domains to $c/a_1/a_2$ domains, and then to a_1/a_2 domains.[12–14] In addition, many other factors, such as depolarizing field, film thickness, external fields and growth conditions, also have an effective impact on the domain pattern in ferroelectric thin films.[19–32] Although multiple growth parameters adjusted are very difficult during the film growth, there are some studies revealing that the film growth conditions (*i.e.*, oxygen pressure, laser frequency, cooling rate, *etc.*) have a significant impact on domain structures and properties.[15,20,24] It is theoretically proposed the cooling rate dependence of domain evolution in terms of kinetically limited phenomena.[25] Since the paraelectric to ferroelectric transformation is nucleation limited, higher cooling rates may suppress nucleation and thus lead to lower transformation temperatures and smaller a-domain volume fractions.[26]

Nevertheless, experimental observations on how the a_1/a_2 domain structures evolve with the cooling rate or other parameters in ferroelectric films have not been reported enough so far, especially at an atomic level. Previously, Cao *et al.* have studied PTO films deposited on MgO(001) by the metal–organic chemical vapor method under different cooling rates and found that a bilayer structure formed in the PTO films, and the bottom layer of the films near the substrate is a-domain region.[27] It implies the effect of cooling rates because it is more likely to form c-domains in PTO/MgO(001) systems due to the large thermal expansion coefficients of MgO than PTO above T_c.[25] In addition, previous studies of a_1/a_2 domain structures have been mainly carried out by piezoresponse force microscope (PFM), which indeed give some macroscopic or mesoscopic information but cannot provide enough atomic-scale information of domain and domain wall patterns due to the lower resolution limitation.[28,29] Therefore, detailed atomic-scale analysis of domains/domain walls evolution *versus* cooling rate in ferroelectric PTO thin films is necessary to better understand the formation mechanism of the domain/domain wall structure and their influence on the electric performances.

In this work, PTO films with a fixed thickness of 40 nm were grown on an orthogonal (110)-oriented $NdScO_3$ (NSO) substrate under different cooling rates and systematically studied by using XRD, TEM and PFM. The NSO substrate is in-plane anisotropic and thermally insensitive undergoing no structural phase transition below 1000 °C.[33] The XRD and TEM investigations indicate periodic stripe a_1/a_2 domains form in these films with domain wall lying on (110) or $(1\bar{1}0)$ of PTO and the domain size decreases along with the cooling rate increases. Moreover, atomically resolved STEM imaging demonstrates that the a_1/a_2 domain structures have salient features under different cooling rates. PFM measurements show that the piezoresponse amplitude is significantly enhanced in PTO films with the fast cooling rate due to the high density domains/domain walls and complex configurations.

2. Experimental section

2.1 Film growth conditions

The PTO thin films with the thickness of 40 nm were grown on NSO single crystal substrates by pulsed laser deposition (PLD), using a 248 nm KrF excimer laser. The PTO target is 3 mol% lead-enriched sintered ceramic. Before film deposition, the NSO substrate was heated to 850 °C for 5 min to clean the substrate surface and then kept at 700 °C. The PTO target was pre-sputtering for 30 min to clean the surface. During the growth of the PTO film, an oxygen pressure of 10 Pa, a laser energy density of 2 J cm^{-2} and a repetition rate of 4 Hz were used. After deposition, the film was stabilized at 700 °C for 5 min in an oxygen pressure of 3×10^4 Pa and then cooled down to room temperature at cooling rates of 5 °C min^{-1}, 15 °C min^{-1}, 30 °C min^{-1}, respectively.

2.2 Characterization studies of films

X-ray diffraction (XRD, the 2θ range of 17–47° with a Cu Kα radiation, $\lambda = 1.5418$ Å) was used to examine the crystalline quality of the films. Piezoresponse force microscopy (PFM) measurements were performed in a scanning probe microscope (Cypher, Asylum Research) using the dual AC resonance tracking (DART) mode. Conductive silicon cantilevers with Ti/Ir coating (Asylum Research, Asyelec-01-R) were used for PFM hysteresis loop measurements. The tip radius is 25 ± 10 nm and the force constant is ≈ 2.8 N m^{-1}.

2.3 Samples preparation, images collection and dates process

Cross-sectional and plan-view samples were prepared by slicing, grinding, dimpling and finally ion milling by using Gatan 691 PIPS, while plan-view samples were milled only from the substrate side. The final ion milling voltage was less than 0.3 kV to reduce amorphous layer produced by ion beam damage. A Tecnai G^2 F30 transmission electron microscope was used for electron diffraction and diffraction contrast analysis. The HAADF-STEM image was acquired using a Titan G^2 60–300 microscope with a high-brightness field-emission gun and double aberration (Cs) correctors from CEOS operating at 300 kV, while the beam convergence angle was 25 mrad and collection angle ranged from 50 mrad to 250 mrad. Strain analysis was based on custom plugins of geometry phase analysis (GPA), carried out using Gatan Digital Micrograph software.[34] Determination of the positions of atoms in the atomic-resolution STEM images was based on Matlab software by two-dimensional (2D) Gaussian peak fittings.[17–19,35–37]

3. Results

The $PbTiO_3$ films were grown on $NdScO_3$ $(110)_O$ substrates (where subscripts O refer to the orthorhombic unit cells). For simplicity, all the orientations without marking subscripts represent pseudocubic perovskite and [001] orientation indicates the out-plane direction which is the direction of film growth. NSO has an orthorhombic crystal structure which

provides two in-plane strain: the NSO in-plane lattice parameters are 4.002 Å (100) and 4.014 Å (010),[33] which produce nominal room temperature misfit strains ε_s of 2.7% and 3% tensile strain, respectively. For PTO ($a = 3.894$ Å, $c = 4.14$ Å),[38] the average mismatch strain is therefore about 2.85%, which is considered to be a large tensile strain.

Fig. 1(a) shows typical XRD θ–2θ scan patterns of the PTO films grown on the NSO substrates with different cooling rates (cooling rates of 5 °C min^{-1}, 15 °C min^{-1}, 30 °C min^{-1}, labeled as T5, T15 and T30 for short). It is seen that all the films are well crystallized into a single perovskite structure and there is no indication of impurity phases. The peak $2\theta = 22.78°$ corresponds to the 100/010-oriented $PbTiO_3$ bulk, and all the systems are in good correspondence with it. The strong peaks are from K_α radiation and indexed as NSO 200 and PTO 200/020 *etc.* The two weak peaks indicated by yellow and green vertical arrows are the K_β peaks of NSO 200 and PTO 200/020, respectively. In addition, the strong and sharp PTO (100)/(010) diffraction peaks indicate that these films are a-domain dominated. The weak PTO (001-oriented) diffraction peaks observed in these films imply a small amount of c-domains embedded in matrix a-domains. In order to further analyze the stripe domains, electron diffraction experiments are carried out on cross-sections of sample T5. Fig. 1(b) is a superposed selected area electron diffraction pattern (SAEDP) taken from the area containing both the PTO film and NSO substrate along the [100] zone axis. Some spots splitting is identified in the pattern, as outlined with the white rectangles. To better visualize the spot splitting, enlargements of the rectangles are shown as insets with the out-of-plane (002) diffraction spots labeled as 1 and in-plane ($0\bar{2}0$) diffraction spots labeled as 2. It is seen that the spots splitting along the [001] direction in enlargement frame 1 can be identified as 002_s and 002_a, which is due to the difference in out-of-plane lattice parameters of PTO and NSO. The subscript "s" denotes substrate and "a" denotes a-domain whose *a*-axis along the out-of-plane direction. The lattice parameter of PTO derived from the diffraction pattern is approximately 0.387 nm, smaller than NSO (0.396 nm) and close to the *a*-axis lattice constant of PTO bulk ($a = 0.389$ nm). The in-plane spots splitting along the [$0\bar{1}0$] direction in enlargement of frame 2 can be determined as $0\bar{2}0_s$ and $0\bar{2}0_a$, respectively. Detailed observation upon (013) indicates that the spot splits into three as seen in Fig. 1(b). The strong spot is from NSO and the two weak spots from two a-domains whose *c*-axis along [010] and [100] direction, respectively.

Fig. 2 displays the cross-sectional TEM images of PTO thin films with different cooling rates grown on NSO substrates. The thickness of the film is about 40 nm. Fig. 2(a) is the bright field image of the T30 PTO film, where it is seen that the interface of film/substrate is flat as marked with a pair of white arrows. Some bright and dark stripe-like areas are regularly distributed, nearly perpendicular to the interface. Fig. 2(b) is a dark-field image corresponding to Fig. 2(a). It is seen in both Fig. 2(a) and (b) that these dark and bright contrast areas are periodically distributed in the film with the width (W) of about 24 nm. Most of the stripes are very narrow, few areas are wide as indicated by the white vertical white arrows, which should be the bifurcations of different domains. Decreasing the cooling rate to T15, the morphology of the PTO films are shown in Fig. 2(c and d) which are a bright field image and corresponding dark field image, respectively. In contrast to the aforementioned features in Fig. 2(a and b), it is seen that some stripe-like areas become wider, and the average width (W) of stripe-like areas increases to be around 26 nm. Further reducing the cooling rate to T5, the morphology changes accordingly as shown in Fig. 2(e and f). In Fig. 2(e and f), it is observed that the stripe-like areas turn to be very sharp, with uniform width (W) of 28 nm. Usually, the a/c domain wall lies on the {011} and {101} twin planes of the $PbTiO_3$, while the a_1/a_2 domain wall lies along the {110} twin planes. In the cross-sectional view, a/c domain wall exhibit

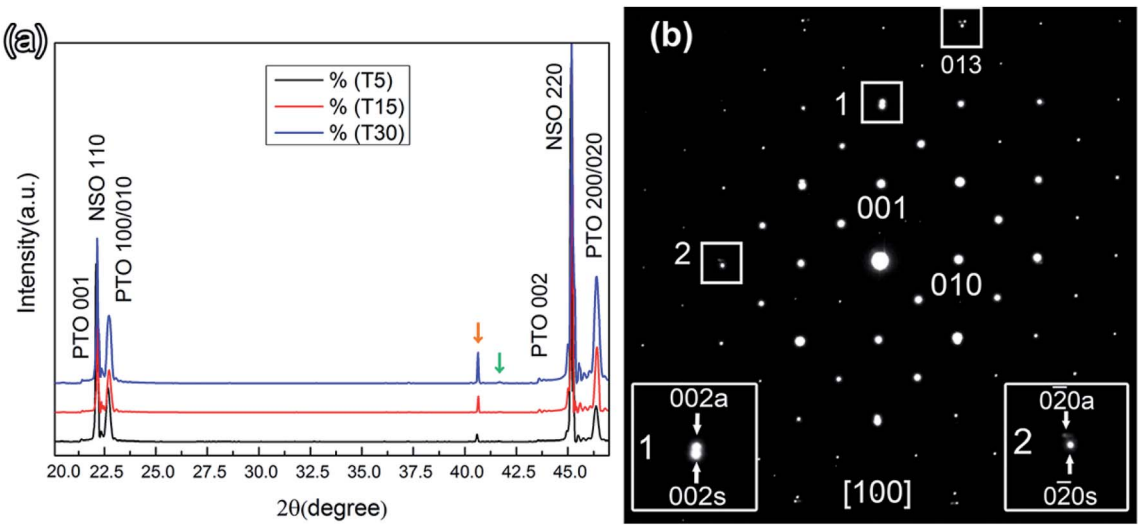

Fig. 1 (a) XRD θ–2θ scan patterns of PTO thin films with different cooling rates grown on NSO substrates. Indexed peaks are K_α of both NSO and PTO; the yellow and green vertical arrows indicate the K_β peaks of NSO 220 and PTO 200/020, respectively. (b) Selected area electron diffraction (SAED) pattern of the T5 PTO film on NSO substrate taken from the area including the film and substrate along [100] zone axis.

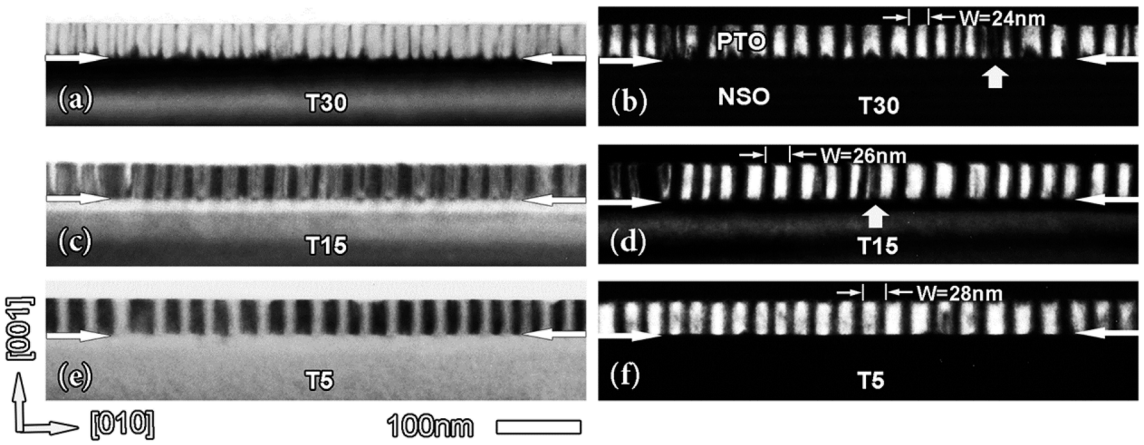

Fig. 2 Cross-sectional images of PTO thin films with different cooling rates grown on NSO substrates. (a), (c), (e) are bright field TEM images and (b), (d), (f) are dark field TEM images. The interface is marked with a pair of horizontal white arrows. Vertical arrow represents the bifurcations of different domains. *W* represents the width of the a_1/a_2 domain structure.

a sharp fringe contrast because they form an angle of 45° with respect to the interface and parallel to the [100] direction; while the a_1/a_2 domain walls are normal to the interface and exhibit a blunt fringe contrast because they form an angle of 45° with respect to the [100] direction. The typical feature is shown in Fig. 2 is vertical stripe-like contrast, which might come from 180° stripe domains, a_1/a_2 domains, threading dislocations or other defects. If these contrasts are from 180° domains, domain walls should be much sharp. Since a-domain is easy to form under large tensile strains and turn into a_1/a_2 domain structure as proposed previously,[12–14] the stripe-like contrasts normal to the interfaces shown in Fig. 2 should be a_1/a_2 domains. Moreover, the XRD study indicates the film is a domain dominated, which also implies these stripes could be 90° a_1/a_2 domains.

As shown in Fig. 2, the domain structure features a periodic $a_1/a_2/a_1/a_2\ldots$ arrangement in each system. In order to explore the thermal evolution of these domain configurations in the films, further study is performed under plan-view observations, as shown in Fig. 3. In Fig. 3(a) (T30), it is seen that the stripe-like areas with alternately bright and dark contrast along [110] or [1$\bar{1}$0] direction are believed to be a_1/a_2 domains (the domain walls are marked with a pair of red dashed lines). To precisely gauge the width of the a_1/a_2 domain (*W*), we measure the perpendicular distance of the domains along [110] or [1$\bar{1}$0], as indicated by a pair of red arrows in Fig. 3. The domain walls both arranged along [110] and [1$\bar{1}$0] directions are approximately equal and the density is high. There are a few discrete bifurcations parallel to the domain wall and the width of the domain change as indicated with the green oval. It is of special interest to notice that there are some special domain features, such as square frame labeled as 1 and 2, each of which are extracted from the image and illustrated in Fig. 3(b, c) and (d, e), respectively. Based on the image in Fig. 3(b) and it's schematic in Fig. 3(c), it is seen that, between the long domains, some tiny domains perpendicular to the longer ones are formed. From Fig. 3(d and e), it is seen that a square domain pattern formed, which is very special and has not been reported before. Decreasing the cooling rate to 15 °C min^{-1}, the domain pattern changed with the domain walls. More dominantly along [110] direction than [1$\bar{1}$0], direction as shown in Fig. 3(f). The width of the domain is not very unanimous and some interaction areas between adjacent domains become obscure. From Fig. 3(g and h) (corresponding to frame 1′), it is seen that some small domains are becoming bigger and more new domains are formed. And from Fig. 3(i and j) (corresponding to frame 2′), the square domain patterns are broken due to the new patterns evolved with the thermal changing. There are some bifurcations appeared in the T15 PTO film. As the cooling rate continues to decrease to 5 °C min^{-1} (T5), it is observed that the domain walls become very sharp and the domain arrangements are highly anisotropic, giving rise to long domain walls as shown in Fig. 3(k). The domains in frame 1″ appear longer than those in T30 and T15 films along [1$\bar{1}$0]. According to the image contrast of area 1″, a selected part of the frame in Fig. 3(l), it is proposed that the different orientation domains intersect and form a threefold vertex distribution as that in the schematic of Fig. 3(m) and will be confirmed later. In the frame labeled as 2″, the square domain patterns are also formed, and relevant information can be clearly found in the corresponding frame (Fig. 3(n)) and schematic (Fig. 3(o)). There are some parallel domains appearing inside the yellow frame, and the arrangements different from the Fig. 3(d)'s. Fig. 3(k) shows more bifurcations, which results from the fact that the width of the domain continuously changes when the cooling rate decreasing.

To establish the relationship between the domain width (*W*) and the cooling rate, we measure the period of domains in both cross-sectional and plan-view samples. The periodicity is measured perpendicular to the domain wall in plan-view observations, whereas in cross-section samples it is measured parallel to the sides of the stripes and hence at 45° to the domain wall. Thus, a $\sqrt{2}$ correction factor has to be included in the comparison. With this correction, the statistics data are summarized in Fig. 4. It is seen that the widths of a_1/a_2 domains

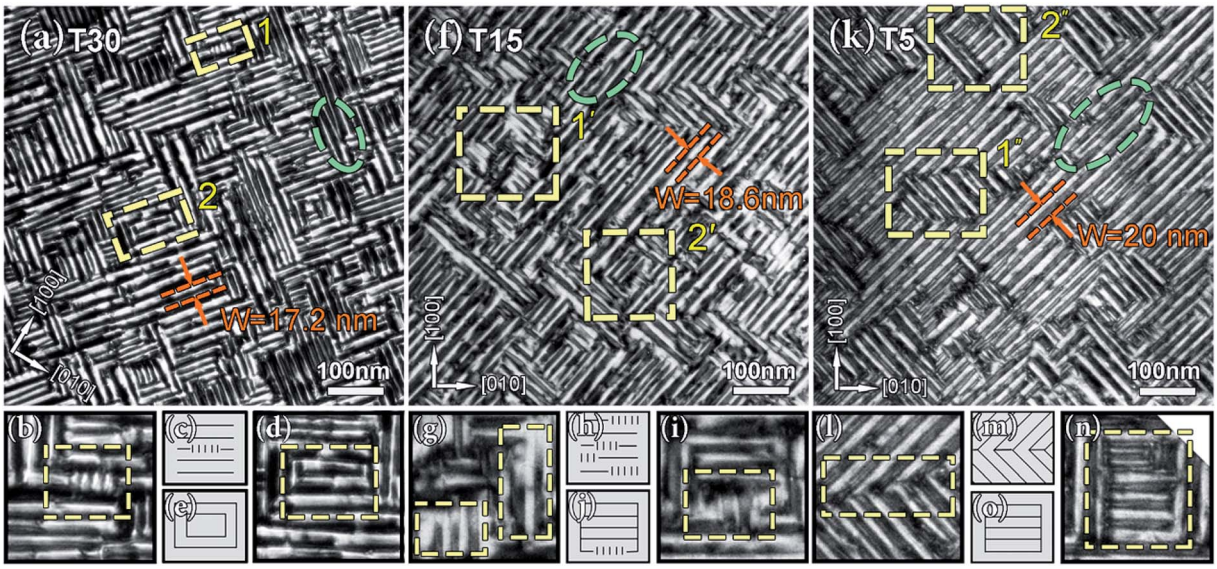

Fig. 3 Plan-view TEM images of the PTO films with different cooling rates on NSO substrates. (a), (f) and (k) are overall topographies of T30, T15 and T5 PTO film. (b)–(e), (g)–(j) and (l)–(o) are local topographies and corresponding schematics of films. The a_1/a_2 domain wall is marked with a pair of red dashed lines and arrows. *W* represents the width of a_1/a_2 domain patterns. Yellow frames labeled as 1, 1′, 1″ represents the growth evolution of a_1/a_2 domain patterns with different domain wall orientations under different cooling rates. Yellow frames labeled as 2, 2′, 2″ represent the evolution of square-framed domain patterns under different cooling rates. Green oval represents the bifurcation of different domains.

increase with decrease the cooling rate. Therefore, the density of domain/domain wall in T30 PTO films is higher than the T15 and T5 PTO films.

To clearly reveal the details of a_1/a_2 domain pattern, high-resolution HAADF-STEM imaging is carried out by aberration-corrected scanning transmission electron microscopy (STEM), which is a very useful tool for studying ionic displacement in perovskite materials. Fig. 5(a) is a low-magnification high-resolution HAADF-STEM image showing the intersections of a_1/a_2 domains with different orientations in T5 PTO films from plan-view observation. The blue dashed lines labeled the 90° a_1/a_2 domain walls, while the red dashed lines traced the 180° domain walls. In tetragonal PTO films, the spontaneous polarization (P_s) projection is opposite to the sub-lattice Ti displacement direction which can be used to determine the polarization of each unit cell.[17–19] Fig. 5(b) is a superposition of reversed d_{Ti} vectors (yellow arrow) with the atomic mapping corresponding to the area labeled with a white rectangle in Fig. 5(a). Red arrows denote reversed d_{Ti} vectors which are consistent with the spontaneous polarization direction of PTO. In the HAADF images, the Pb^{2+} columns appear as the bright dots because the intensity of atom columns is approximately proportional to $Z^{1.7-2}$, where Z is the atomic number,[17–19,35,36] while the Ti^{4+} columns show weak contrast. It is noteworthy that the two 90° domain walls and one 180° domain wall actually generate a threefold vertex domain (Fig. 5(b)). To map the strain distribution around a_1/a_2 domains, geometric phase analysis (GPA) is carried out corresponding to Fig. 5(a).[34,36,37] Fig. 5(c) is the in-plane strain (ε_{xx}) map, where it is seen that the in-plane strain distribution is inhomogeneous. This is due to the difference of *c*-axis orientations of a_1/a_2 domains, consequently, the a_1/a_2 domain walls can be easily distinguished according to the different colors (the in-plane strain in the a_1 domain is set to be zero). Fig. 5(d) shows the in-plane lattice rotation (R_x) map, corresponding to the area shown in Fig. 5(a). The yellow arrow as seen in Fig. 5(a) and (d) indicates a 180° and 90° domain wall, which is similar to the previous observations.[22,37]

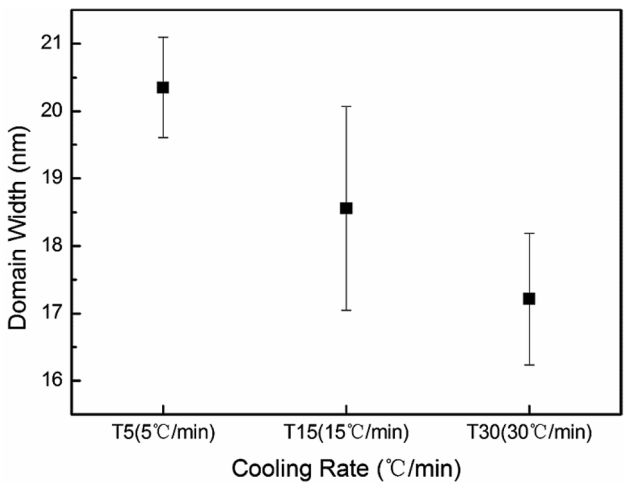

Fig. 4 The cooling rates dependence of the a_1/a_2 domain width (*W*). The data is statistically obtained from numerous domains in both cross-sectional and plan-view samples.

It is worthwhile to mention that the sample with a fast cooling rate (T30) exhibits distinct characteristics. Fig. 6(a) is a low-magnification high-resolution HAADF-STEM image showing the domain distribution in T30 films obtained from

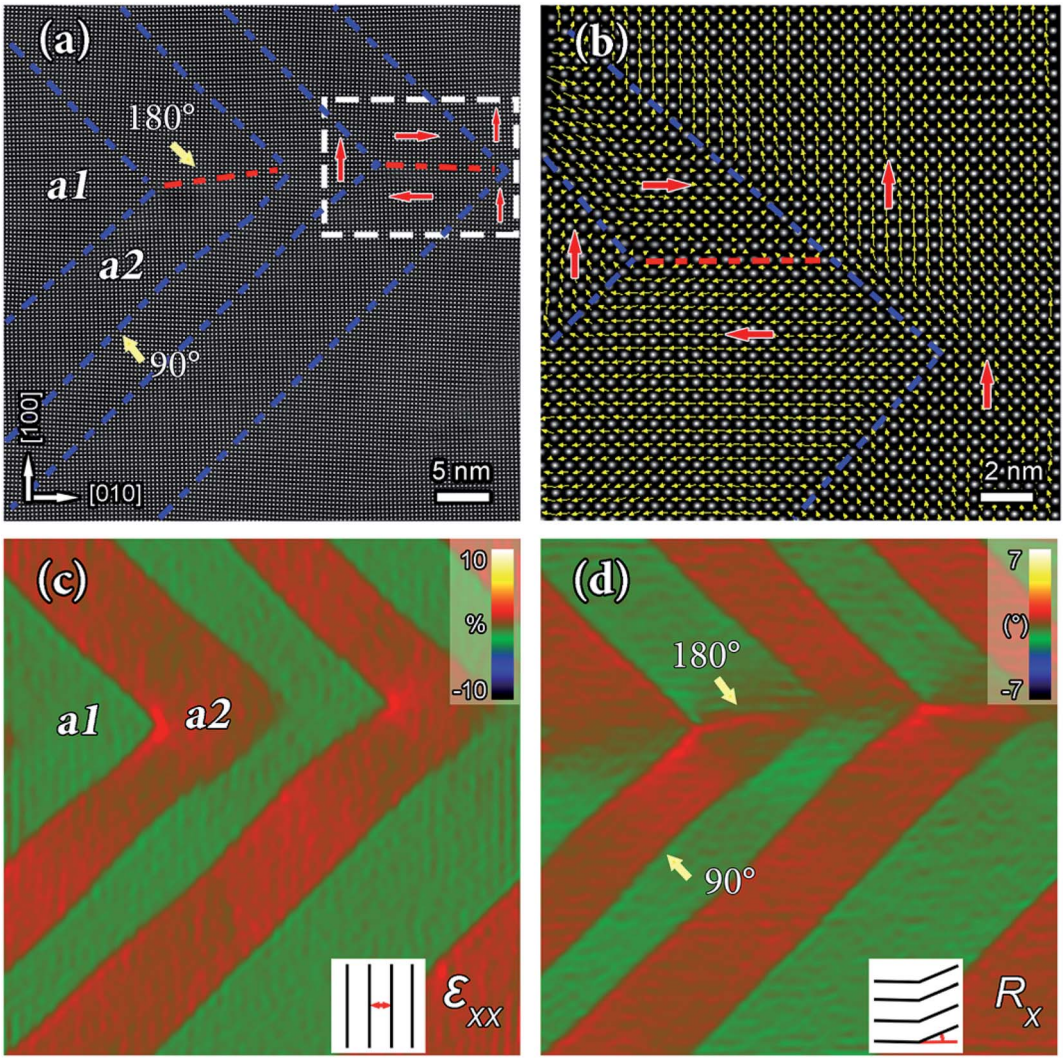

Fig. 5 (a) A low magnification plan-view high-resolution HAADF-STEM image showing uncharged domain patterns in T5 PTO films. (b) Superposition of reversed d_{Ti} vectors (yellow arrow) with the atomic mapping of the area labeled with a white rectangle in (a). (c) GPA of in-plane strain (ε_{xx}) and (d) in-plane lattice rotation (R_x) map of (a). The yellow arrow indicates the 180° and 90° domain walls, respectively. In (a) and (b), blue dashed lines are used to indicate 90° domain walls, while red dashed lines represent 180° domain walls; red arrows denote reversed d_{Ti} vectors which are consistent with the spontaneous polarization direction of PTO. In (c) and (d), the insets show schematic representations of the lattice deformations measured in each map.

plan-view. It is seen that the a_1/a_2 domains along [110] and [1$\bar{1}$0],direction are arranged regularly and the domain density is very high. In addition to the a_1/a_2 domains, some complex domain configurations such as square frame-like domain patterns are observed as indicated with a white frame. Fig. 6(b) is an atomically resolved HAADF-STEM image of the area labeled as a white frame in Fig. 6(a), where the blue dashed lines indicate the domain walls. It is seen that the complex domain pattern consists of five domains named a_0–a_4. To figure out the strain and polarization distributions around the domains, in-plane strain mapping by GPA is conducted and shown in Fig. 6(c). The in-plane strain (ε_{xx}) map show the inhomogeneous distributions due to the coupling between the distortion lattice and the polarization. The a_1/a_2 domain walls can be easily distinguished due to the colors difference (the in-plane strain in a_0 domain is set to be zero). In Fig. 6(c), four domains (red area) formed a square frame-like domain pattern, and one domain with frame-like (blue area) is enclosed by the others. To figure out the polarization distribution, two areas are selected as indicated by white frames in Fig. 6(b). According to the polarization distributions shown in Fig. 6(d and e), it is seen that the upper white frame (labeled as 1) indicates a presence of a "tail-to-tail" domain wall, while the lower white frame (labeled as 2) displays an existence of a "head-to-head" domain wall. The unmarked areas in the left and right have similar domain wall types, *e.g.* 180° domain wall. According to the strain distribution in Fig. 6(c) and polarization distributions in Fig. 6(d and e), the schematic diagram of polarization distribution in the square frame-like patterns is illustrated in Fig. 6(f). It is worthwhile to mention that the presence of the charged domain wall might

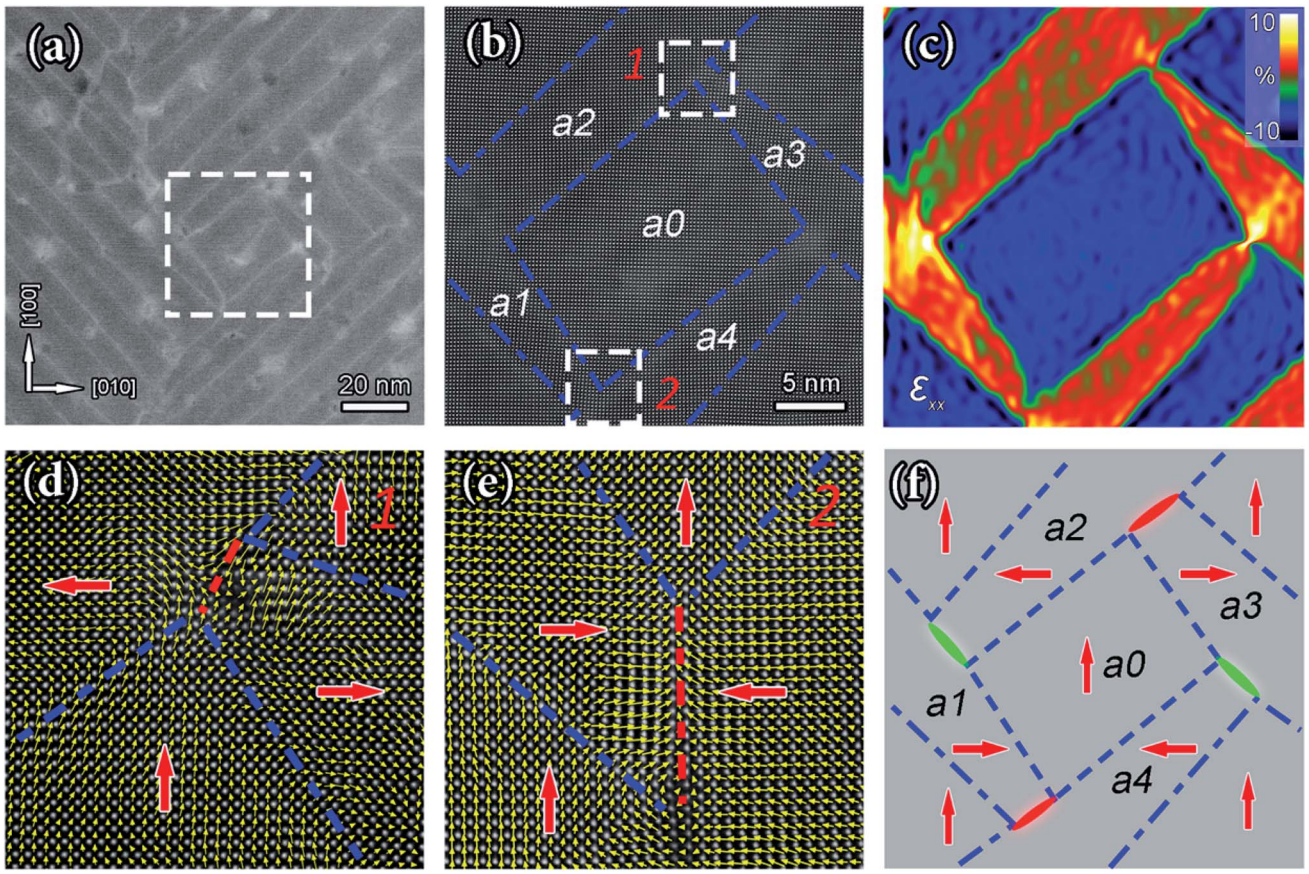

Fig. 6 (a) A low-magnification plan-view high-resolution HAADF-STEM image showing the charged domain patterns in the T30 PTO film. (b) A high-resolution HAADF-STEM image of the area labeled with a white frame in (a), the blue dashed lines indicate the domain walls. (c) GPA of (b) in-plane strain (ε_{xx}) map. (d) and (e) Superposition of reversed d_{Ti} vectors (yellow arrow) with the atomic mapping of the upper white frame 1 and lower white frame 2, respectively. Red arrows denote reversed d_{Ti} vectors which are consistent with the spontaneous polarization direction of PTO. (f) Schematic diagram of polarization distributions of (b) according to (d and e). In (d–f), blue (or green) and red dashed lines (or ovals) labeled as uncharged and charged domain walls, respectively.

induce unusual structural distortions and exotic physical properties.[39,40]

For the PTO films with different cooling rates, the phase–voltage hysteresis loops in Fig. 7(a) shows a well-defined square loop feature and the amplitude–voltage hysteresis loops in Fig. 7(b) displays a typical "butterfly shape". These performances suggest the existence of ferroelectric switch behavior in these PTO thin films.[41,42] Importantly, the T30 PTO film has a maximum piezoresponse amplitude compared with others, implying a higher piezoelectric response. The T15 and T5 PTO films have relatively lower piezoresponse amplitudes, which indicate that the piezoelectric response is dependent on domain density and configurations.

4. Discussion

The tetragonal PTO films, deposited onto an NSO orthogonal substrate, are strained and consequently exhibit different in-plane lattice constants. Even a slight difference in the in-plane lattice mismatch is sufficient to influence the domain structure.[30,32] The anisotropy of the substrate's in-plane lattice constants can influence the domain formation energy barrier during PE–FE transformation. Although the stability maps provide a general and versatile approach for understanding the final domain configurations, the relaxation kinetics after the PE–FE transformation also need to be taken into account when growth conditions change. The difference of domain width in the different cooling rate systems can be ascribed to the different growth kinetics of the domain during the film deposition. But it should be pointed out that the final pattern of the domain with the fast cooling rate (T30) is determined by growth kinetics, which means that there is not enough time and energy for the nucleation growth. So the variants of the domain are randomly distributed in the two in-plane directions. In the meanwhile, the cooling rate also can influence the formation of mobile point defects (such as oxygen vacancies).[36] Populations of the point defects could be pinned on the domain walls, resulting in the increment of total energy and thus the novel domain patterns formed. Generally, a_1/a_2 domains are 90° domains and their polarizations are in-plane, which suggest that their formation is not driven by depolarization field. Instead, it is related to an attempt to minimize stress in the film.

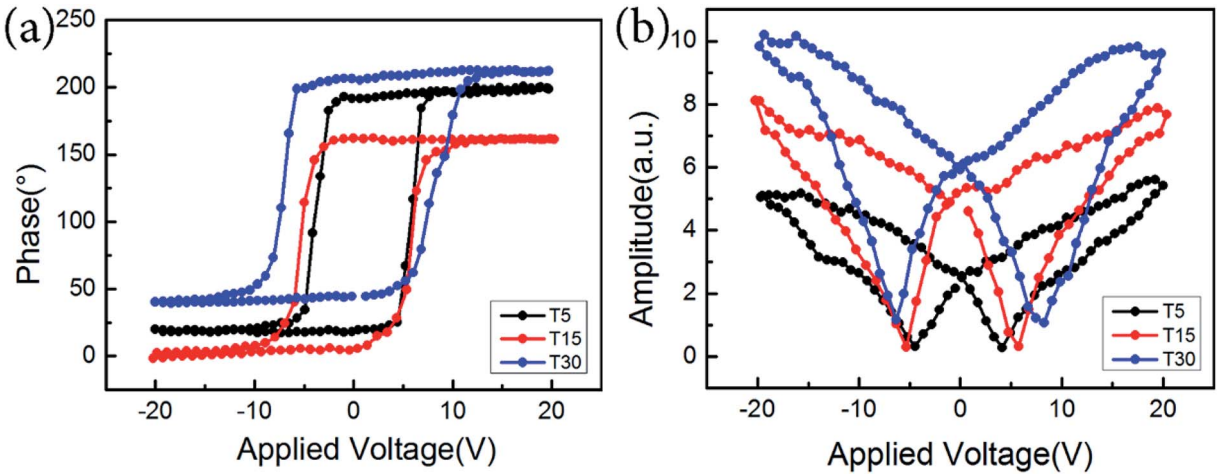

Fig. 7 Local PFM hysteresis loops of the PTO thin films with different cooling rates grown on NSO substrates. (a) Phase–voltage and (b) amplitude–voltage piezoresponse hysteresis loops.

In spite of the obvious lattice distortion and broadening at the domain walls. There also are some charged domain wall formation here, which may be related to the fast cooling rate because charged domain walls are not the most favourable configurations,[43] which might be stabilized by electrostatic energy and mechanical forces. Such mechanical forces stem from substrate clamping and mutual forces that are induced by the domains during the crystallographic phase transition.[40] Furthermore, the final patterns of the domain in the slow cooling rate system (T5) is determined by thermodynamic. It is observed that the single domain variant becomes more favourable when the cooling rate decreases, leading to the domains longer and wider along one orientation. The reason may lie in two factors. One is the elastic energy. As the system cooling rate decreases, the elastic energy is associated with the formation of walls between the domain variants decrease; the other one is the point defect relaxation. As the system cooling rate decreases, the point defect diffusional processes increase. As a result, a single domain state is energetically more favourable. Along with the cooling rate decreases from T30 to T15 and then to T5, the domain size tends to large. This phenomenon implies that the manner of strain relaxation in the films is associated with domain wall motion, such as coalescence of adjacent domain. Therefore, it is more or less prone to be the one classified as Ostwald ripening-like structures.[44] In fact, the final domain state depends on the competition between various energies associated with exchange and crystallographic anisotropy of ferroelectric materials.

In addition, the width of the domain decreases when the film cooling rate increases, which results in a higher density of domain walls. As in the previous studies, the high density of domain walls can enhance the response to the applied electric field of the films.[30,31,41,45] In the present study, the slower cooling rate leads to the bigger domain size and less volume fraction of domain walls, which implies that the domain wall motion and domain switching exhibit lower negative/positive coercive fields compared with that of the T15 and T30 PTO films as indicated in Fig. 6(b). This is because the smaller the domain size and the larger the ratio of the domain wall, which is able to reduce the switching behaviours of the domain. In this case, a higher field is needed to induce the domain wall motion and domain switching.

Furthermore, it is known that the piezoelectric effect of thin films is strongly associated with domain patterns, crystal structure and crystallographic orientation.[30,31,46] In the PTO thin film with fast cooling rate, the square frame-like domain patterns formed with distorted charged domain wall. Although the Landau–Ginzburg theory suggests that charged walls should be unstable,[43] a small amount of charged domain wall could be sufficient to account for the enhancement of the piezoelectric effect in domain engineered tetragonal ferroelectric crystals, such as $BaTiO_3$, $PbTiO_3$.[46] Generally, it is proposed that the charged domain wall is wider than the neural domain wall, and the polarization should change gradually in the domain wall to relax the strain between domains.[47–49] Thus, an increase in the volume fraction of the distorted domain wall region result in the high piezoelectric response.

5. Conclusions

In this study, we show that it is possible to tune the a_1/a_2 domain size and domain patterns by controlling the epitaxial deposition conditions. Our results provide direct evidence that the a_1/a_2 domain size increases with the cooling rate decreases, and the domain patterns evolved from simple uncharged domains to complex charged domains. It is proposed that the charged a_1/a_2 domain patterns in PTO films with fast cooling are determined by growth kinetics, while the films with a slow cooling rate are governed by thermodynamic. The PTO film with fast cooling rate shows high piezoresponse due to the high density of domains/walls and amount of distorted charged domain wall.

Conflicts of interest

There are no conflicts to declare.

Acknowledgements

This work is supported by the Key Research Program of Frontier Sciences CAS (QYZDJ-SSW-JSC010), the National Natural Science Foundation of China (No. 51671194, No. 51571197), and National Basic Research Program of China (2014CB921002), Y. L. T. acknowledges the IMR SYNL-T. S. Kê Research Fellowship and the Youth Innovation Promotion Association CAS (No. 2016177). We are grateful to Mr B. Wu and Mr L. X. Yang of this lab for their technical support on the Titan platform of G^2 60–300 kV aberration-corrected scanning transmission electron microscope.

References

1 D. Dragan, *Rep. Prog. Phys.*, 1998, **61**, 1267.
2 J. F. Scott, *Science*, 2007, **315**, 954.
3 Z. Pavlo, C. W. Jacek, H. Marios, F. P. Stéphanie, S. Anais, L. Igor, M. T. Jean and Í. Jorge, *Nature*, 2016, **534**, 525.
4 P. Zubko, H. D. Lu, C. W. Bark, X. Martí, J. Santiso, C. B. Eom, G. Catalan and A. Gruverman, *J. Phys.: Condens. Matter*, 2017, **29**, 284001.
5 L. Xie, L. Z. Li, C. A. Heikes, Y. Zhang, Z. J. Hong, P. Gao, C. T. Nelson, F. Xue, E. Kioupakis, L. Q. Chen, D. G. Schlom, P. Wang and X. Q. Pan, *Adv. Mater.*, 2017, **29**, 1701475.
6 V. Nagarajan, A. Roytburd, A. Stanishevsky, S. Prasertchoung, T. Zhao, L. Chen, J. Melngailis, O. Auciello and R. Ramesh, *Nat. Mater.*, 2003, **2**, 43.
7 J. Seidel, L. W. Martin, Q. He, Q. Zhan, Y. H. Chu, A. Rother, M. E. Hawkridge, P. Maksymovych, P. Yu, M. Gajek, N. Balke, S. V. Kalinin, S. Gemming, F. Wang, G. Catalan, J. F. Scott, N. A. Spaldin, J. Orenstein and R. Ramesh, *Nat. Mater.*, 2009, **8**, 229.
8 Q. L. He, C. H. Yeh, J. C. Yang, G. S. Bhalla, C. W. Liang, P. W. Chiu, G. Catalan, L. W. Martin, Y. H. Chu, J. F. Scott and R. Ramesh, *Phys. Rev. Lett.*, 2012, **108**, 067203.
9 A. Bhatnagar, A. R. Chaudhuri, Y. H. Kim, D. Hesse and M. Alexe, *Nat. Commun.*, 2013, **4**, 2835.
10 G. Arlt, *J. Mater. Sci.*, 1990, **25**, 2655.
11 E. G. Fesenko, V. G. Gavrilyatchenko and A. F. Semenchev, *Ferroelectrics*, 1989, **100**, 195.
12 Y. L. Li, S. Y. Hu, Z. K. Liu and L. Q. Chen, *Acta Mater.*, 2002, **50**, 395.
13 N. A. Pertsev, A. G. Zembilgotov and A. K. Tagantsev, *Phys. Rev. Lett.*, 1998, **80**, 1988.
14 V. G. Koukhar, N. A. Pertsev and R. Waser, *Phys. Rev. B: Condens. Matter Mater. Phys.*, 2001, **64**, 214103.
15 O. Nesterov, S. Matzen, C. Magen, A. H. G. Vlooswijk and G. Catalan, *Appl. Phys. Lett.*, 2013, **103**, 142901.
16 F. Borodavka, I. Gregora, A. Bartasyte, S. Margueron, V. Plausinaitiene, A. Abrutis and J. Hlinka, *J. Appl. Phys.*, 2013, **113**, 187216.
17 Y. L. Tang, Y. L. Zhu, X. L. Ma, A. Y. Borisevich, A. N. Morozovska, E. A. Eliseev, W. Y. Wang, Y. J. Wang, Y. B. Xu, Z. D. Zhang and S. J. Pennycook, *Science*, 2015, **348**, 547.
18 A. K. Yadav, C. T. Nelson, S. L. Hsu, Z. Hong, J. D. Clarkson, C. M. Schlepütz, A. R. Damodaran, P. Shafer, E. Arenholz, L. R. Dedon, D. Chen, A. Vishwanath, A. M. Minor, L. Q. Chen, J. F. Scott, L. W. Martin and R. Ramesh, *Nature*, 2016, **530**, 198.
19 C. T. Nelson, B. Winchester, Y. Zhang, S. J. Kim, A. Melville, C. Adamo, C. M. Folkman, S. H. Baek, C. B. Eom, D. G. Schlom, L. Q. Chen and X. Q. Pan, *Nano Lett.*, 2011, **11**, 828.
20 C. Becher, L. Maurel, U. Aschauer, M. Lilienblum, C. Magén, D. Meier, E. Langenberg, M. Trassin, J. Blasco, I. P. Krug, P. A. Algarabel, N. A. Spaldin, J. A. Pardo and M. Fiebig, *Nat. Nanotechnol.*, 2015, **10**, 661.
21 S. Li, Y. L. Zhu, Y. L. Tang, Y. Liu, S. R. Zhang, Y. J. Wang and X. L. Ma, *Acta Mater.*, 2017, **131**, 123.
22 Y. Liu, Y. J. Wang, Y. L. Zhu, C. H. Lei, Y. L. Tang, S. Li, S. R. Zhang, J. Li and X. L. Ma, *Nano Lett.*, 2017, **17**, 7258.
23 S. R. Zhang, Y. L. Zhu, Y. L. Tang, Y. Liu, S. Li, M. J. Han, J. Y. Ma, B. Wu, Z. H. Chen, S. Saremi and X. L. Ma, *Adv. Mater.*, 2017, **29**, 170354.
24 L. Feigl, P. Yudin, I. Stolichnov, T. Sluka, K. Shapovalov, M. Mtebwa, C. S. Sandu, X. K. Wei, A. K. Tagantsev and N. Setter, *Nat. Commun.*, 2014, **5**, 4677.
25 J. S. Speck and W. Pompe, *J. Appl. Phys.*, 1994, **76**, 466.
26 C. M. Foster, W. Pompe, A. C. Daykin and J. S. Speck, *J. Appl. Phys.*, 1996, **79**, 1405.
27 Y. Gao, G. Bai, K. L. Merkle, H. L. M. Chang and D. J. Lam, *Thin Solid Films*, 1993, **235**, 86.
28 L. J. McGilly, A. Schilling and J. M. Gregg, *Nano Lett.*, 2010, **10**, 4200.
29 R. G. P. McQuaid, L. J. McGilly, P. Sharma, A. Gruverman and J. M. Gregg, *Nat. Commun.*, 2011, **404**, 1413.
30 A. S. Everhardt, S. Matzen, N. Domingo, G. Catalan and B. Noheda, *Adv. Electron. Mater.*, 2016, **2**, 1500214.
31 Y. P. Feng, Y. L. Tang, D. S. Ma, Y. L. Zhu, M. J. Zou, M. J. Han, J. Y. Ma and X. L. Ma, *ACS Appl. Mater. Interfaces*, 2018, **10**, 24627.
32 S. Kobayashi, K. Inoue, T. Kato, Y. Ikuhara and T. Yamamoto, *J. Appl. Phys.*, 2018, **123**, 064102.
33 R. Uecker, B. Velickov, D. Klimm, R. Bertram, M. Bernhagen, M. Rabe, M. Albrecht, R. Fornari and D. G. Schlom, *J. Cryst. Growth*, 2008, **310**, 2649.
34 M. J. Hÿtch, E. Snoeck and R. Kilaas, *Ultramicroscopy*, 1998, **74**, 131.
35 C. L. Jia, S. B. Mi, K. Urban, I. Vrejoiu, M. Alexe and D. Hesse, *Nat. Mater.*, 2008, **7**, 57.
36 P. Gao, J. Britson, J. R. Jokisaari, C. T. Nelson, S. H. Baek, Y. Wang, C. B. Eom, L. Q. Chen and X. Q. Pan, *Nat. Commun.*, 2013, **4**, 3791.
37 Y. L. Tang, Y. L. Zhu and X. L. Ma, *Ultramicroscopy*, 2016, **160**, 57.
38 G. Shirane and S. Hoshino, *J. Phys. Soc. Jpn.*, 1951, **6**, 265.

39 W. Y. Wang, Y. L. Tang, Y. L. Zhu, Y. B. Xu, Y. Liu, Y. J. Wang, S. Jagadeesh and X. L. Ma, *Adv. Mater. Interfaces*, 2015, **9**, 1500024.
40 Y. Ivry, D. P. Chu, J. F. Scott and C. Durkan, *Adv. Funct. Mater.*, 2011, **21**, 1827.
41 R. J. Xu, J. Karthik, A. R. Damodaran and L. W. Martin, *Nat. Commun.*, 2014, **5**, 3120.
42 S. Wada, S. Suzuki, T. Noma, T. Suzuki, M. Osada, M. Kakihana and S. E. Park, *Jpn. J. Appl. Phys., Part 1*, 1999, **38**, 5505.
43 Y. Ishibashi and E. Salje, *Ferroelectrics*, 2004, **303**, 607.
44 C. Sagui, D. Orlikowski, A. M. Somoza and C. Roland, *Phys. Rev. E: Stat. Phys., Plasmas, Fluids, Relat. Interdiscip. Top.*, 1998, **58**, R4092.
45 W. Li, Y. Wang, P. Nie, Q. Hu, Y. Yang and G. Yuan, *Phys. B*, 2015, **466**, 11.
46 W. Wada, K. Yako, H. Kakemoto, T. Tsurumi and T. Kiguchi, *J. Appl. Phys.*, 2005, **98**, 014109.
47 B. Meyer and D. Vanderbilt, *Phys. Rev. B: Condens. Matter Mater. Phys.*, 2002, **65**, 104111.
48 W. F. Rao and Y. U. Wang, *Appl. Phys. Lett.*, 2007, **90**, 041915.
49 Y. L. Tang, Y. L. Zhu, Y. J. Wang, W. Y. Wang, Y. B. Xu, W. J. Ren, Z. D. Zhang and X. L. Ma, *Sci. Rep.*, 2014, **4**, 4115.